Nanotechnology **23** (2012) 095703 (10pp) doi:10.1088/0957-4484/23/9/095703

Radial elasticity of multi-walled boron nitride nanotubes

Meng Zheng[1], Changhong Ke[1], In-Tae Bae[2], Cheol Park[3,4], Michael W Smith[5] and Kevin Jordan[6]

[1] Department of Mechanical Engineering, State University of New York at Binghamton, Binghamton, NY 13902, USA
[2] Small Scale Systems Integration and Packaging Center, State University of New York at Binghamton, Binghamton, NY 13902, USA
[3] National Institute of Aerospace, 100 Exploration Way, Hampton, VA 23666, USA
[4] Department of Mechanical and Aerospace Engineering, University of Virginia, Charlottesville, VA 22904, USA
[5] NASA Langley Research Center, Hampton, VA 23681, USA
[6] Thomas Jefferson National Accelerator Facility, 12000 Jefferson Avenue, Newport News, VA 23606, USA

E-mail: cke@binghamton.edu

Received 21 September 2011, in final form 13 January 2012
Published 6 February 2012
Online at stacks.iop.org/Nano/23/095703

Abstract
We investigated the radial mechanical properties of multi-walled boron nitride nanotubes (MW-BNNTs) using atomic force microscopy. The employed MW-BNNTs were synthesized using pressurized vapor/condenser (PVC) methods and were dispersed in aqueous solution using ultrasonication methods with the aid of ionic surfactants. Our nanomechanical measurements reveal the elastic deformational behaviors of individual BNNTs with two to four tube walls in their transverse directions. Their effective radial elastic moduli were obtained through interpreting their measured radial deformation profiles using Hertzian contact mechanics models. Our results capture the dependences of the effective radial moduli of MW-BNNTs on both the tube outer diameter and the number of tube layers. The effective radial moduli of double-walled BNNTs are found to be several-fold higher than those of single-walled BNNTs within the same diameter range. Our work contributes directly to a complete understanding of the fundamental structural and mechanical properties of BNNTs and the pursuits of their novel structural and electronics applications.

(Some figures may appear in colour only in the online journal)

1. Introduction

Boron nitride nanotubes (BNNTs) [1, 2], one type of one-dimensional nanostructure, have received increasing attention from the research community in recent years. Research has shown that BNNTs possess very high Young's modulus (up to 1.3 GPa) [3–9], excellent thermal conductivity [10, 11], chemical and thermal stability [12, 13], and electrically insulating properties [1, 14, 15], which originate from their repeated and partially ionic B–N bonding network architectures and are comparable, or even superior, to those of carbon nanotubes (CNTs) [16]. Therefore, BNNTs are ideal for applications demanding high strength, thermally and chemically stable and electrically insulating materials. Our recent studies on the radial mechanical properties of single-walled BNNTs (SW-BNNTs) [17] reveal that single-layer cylindrical B–N bonding networks have relatively lower resistance to transverse loads compared with covalent C–C bonding networks, even though their respective resistances to axial loads are reportedly comparable. The axially strong but radially supple characteristics suggest that SW-BNNTs may be superior to their CNT counterparts as reinforcing additives for ceramic nanocomposites [18–21] based on the fact that better conformation of nanotubes to ceramic grains is desired for the improvement of fracture toughness. In addition, the radial rigidity of BNNTs also determines their cross-sectional

configurations in the forms of bundles or ropes [22, 23] or when they are in contact with other material surfaces [24], and has a significant influence on their mechanical deformational behaviors under a variety of loading conditions (e.g. compression, bending, and torsion) [25–27] as well as their electrical properties. It has been recently reported that the bandgaps of BNNTs, originally in the range of 5–6 eV [1, 14, 15], decrease under mechanical deformations [28, 29].

BNNTs can crystallize in both single-walled and multi-walled nanophases. Due to the partially ionic character of B–N bonds, boron and nitrogen atoms are arranged alternately along the tube axis and prefer to form double or multiple-layered tubular structures due to the prominent, so-called 'lip–lip' interaction between neighboring B–N layers [16]. Therefore, structures of multi-walled BNNTs (MW-BNNTs) are considered to be more stable than those of SW-BNNTs, which is supported by the evidence that MW-BNNTs are found to be much more common than SW-BNNTs in the synthesized materials [30]. Due to their more stable structures and better availability, MW-BNNTs have been employed in the majority of experimental studies of fundamental structural and material properties and applications of BNNTs. Therefore, it is of great importance to understand the radial mechanical properties of MW-BNNTs.

Up to date, several methods have been proposed to synthesize BNNTs, such as catalyst based CVD methods [31, 32], arc-discharge methods [2], ball-milling methods [33], and laser heating methods [34–37]. A catalyst-free BNNT growth method named PVC (pressurized vapor/condenser) was recently reported to be capable of producing highly crystalline, very long, and small diameter BNNTs [23]. For the BNNTs synthesized using the PVC method, it is reported that the majority of the tubes have two to five walls, which are ideal materials for studying the radial elasticity of MW-BNNTs.

In this paper, we present a nanomechanical study of the radial elasticity of PVC-synthesized MW-BNNTs. The employed MW-BNNTs were first dispersed in aqueous solution using ultrasonication methods with the aid of surfactants, and their structural configurations were characterized by both high resolution transmission electron microscopy (HRTEM) and atomic force microscopy (AFM) techniques. Then the radial deformations of individual MW-BNNTs with two to four tube walls were characterized by AFM-based nanomechanical testing techniques. Our nanomechanical measurements were interpreted using Hertzian contact mechanics models, and the effective radial elastic moduli of the tested MW-BNNTs were obtained based on their measured radial deformation profiles. Our measurements also reveal the dependence of the BNNT radial rigidity on critical nanotube structural parameters, including the tube outer diameter and the number of tube layers. Our results reported in this paper contribute directly to a complete understanding of the fundamental structural and mechanical properties of BNNTs and the pursuits of their novel structural and electronics applications, such as polymeric and ceramic composites [19, 38], protective shields/capsules [39], and electronics and optoelectronics devices [19, 40].

2. Results and discussion

2.1. Dispersion and structural characterization of BNNTs

The employed PVC-synthesized BNNTs were originally in the form of dry cotton-like fibrils. Figure 1(a) shows a representative scanning electron microscopy (SEM) image of as-grown BNNT material formed by entangled networks of branching nanotubes and tube bundles. For the purpose of performing nanomechanical measurements on individual BNNTs, as-grown BNNTs were first dispersed in deionized (DI) water by ultrasonication with the aid of ionic surfactant sodium dodecylbenzenesulfonate (NaDDBS). NaDDBS, consisting of a benzene ring moiety, a charged group, and an alkyl chain, is known as an effective surfactant for dispersing single- and multi-walled CNTs [41–43]. Figure 1(b) shows three selected pictures demonstrating the effectiveness of NaDDBS in de-bundling and dispersing BNNTs: (1) ∼0.2 mg of as-synthesized BNNTs and ∼0.1 mg of dry-powder NaDDBS were first added in 250 μl of DI water and the mixture was then ultrasonicated for 1 min. The solution became pale in color and BNNT aggregates were observed at the bottom of the solution. (2) The solution turned into a white color and became relatively uniform after ten-minute ultrasonication. The amount of BNNT aggregates at the bottom of the solution was greatly reduced. (3) The solution became more uniform and limpid after one-hour ultrasonication. We also performed control experiments of ultrasonicating the mixture of as-grown BNNTs and DI water, without the addition of NaDDBS, under the same conditions. No discernable change to the BNNTs in the solution was observed after one-hour ultrasonication, indicating that BNNTs could not be effectively dispersed or de-bundled in DI water just by means of ultrasonication. Our results clearly demonstrate that NaDDBS is an effective surfactant in dispersing BNNTs. It is noted that another type of ionic surfactant, ammonium-oleate, was previously reported for the dispersion of MW-BNNTs in aqueous solution [44].

The supernatant of the dispersed BNNTs was characterized using both HRTEM and AFM. Our HRTEM characterization captured both SW- and MW-BNNTs whose diameters were mostly within the range of 1–6 nm. Among MW-BNNTs, double-walled tubes were the most frequently observed tubular structures. Figure 1(c) shows a representative HRTEM image of BNNTs in the form of double-wall and triple-wall configurations, while the inset image shows a quadruple-walled BNNT (QW-BNNT). Figure 1(d) shows the outer diameter ranges of single- to quadruple-walled BNNTs captured by HRTEM. The outer diameter range of the observed double-walled BNNTs (DW-BNNTs) is found to be from 2.0 to 4.0 nm ($n = 47$), while 0.7–2.4 nm for SW-BNNTs ($n = 6$), 2.8–5.6 nm for triple-walled BNNTs (TW-BNNTs) ($n = 17$) and 3.7–6.6 nm for QW-BNNTs ($n = 7$). It can be clearly seen from the data presented in figure 1(d) that the diameter range of one type of BNNT partially overlaps with other types of tubes. Therefore, the exact wall number of a BNNT may not be directly identified based on its outer diameter when it falls into the overlapping

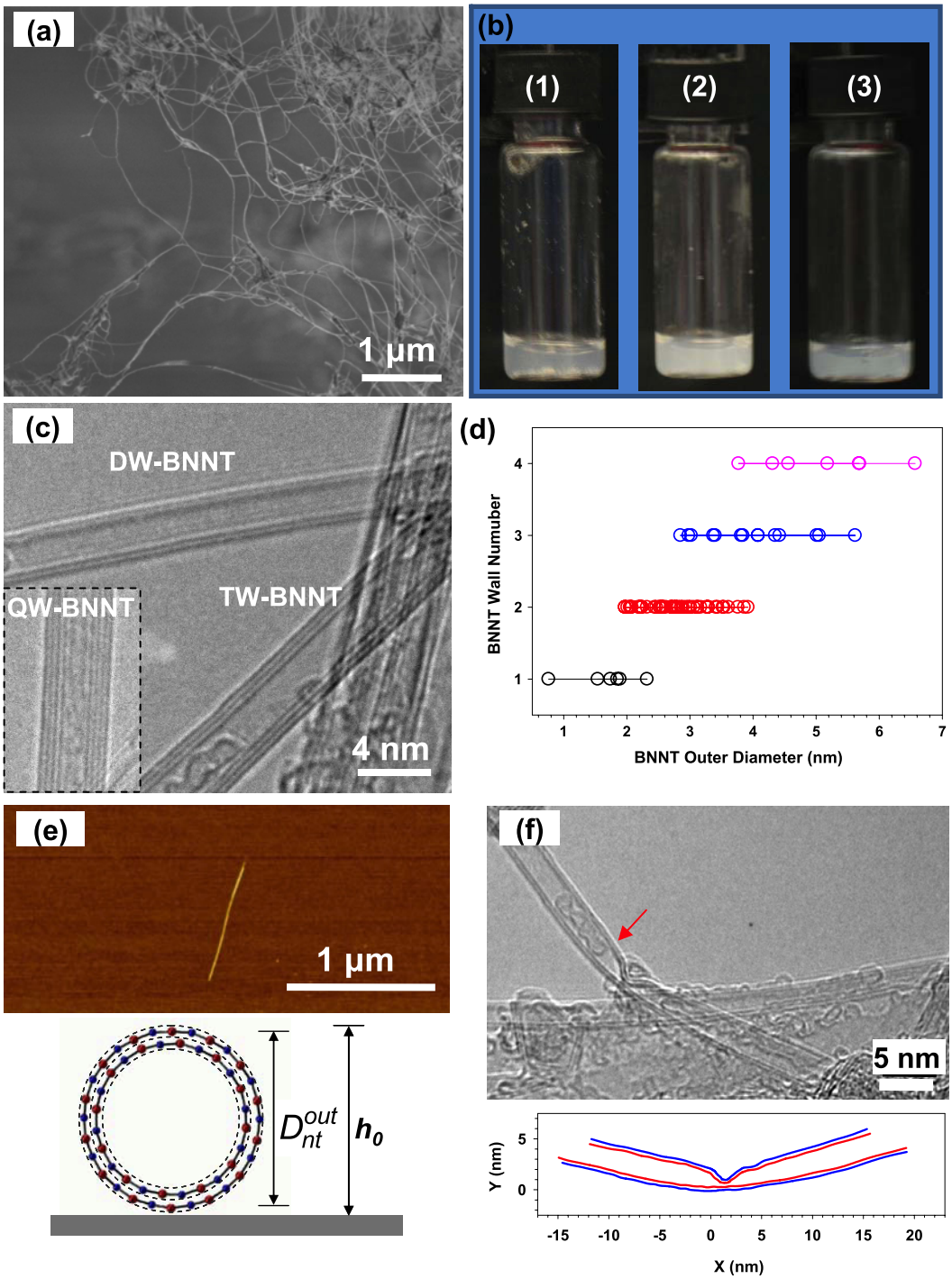

Figure 1. (a) SEM image of as-synthesized BNNTs using PVC methods. (b) Three selected pictures showing the processes of dispersing BNNTs in aqueous solution with the aid of surfactant NaDDBS: (1) as-grown BNNTs were first added to the DI water with NaDDBS and the mixture was then ultrasonicated for 1 min; (2) the BNNT solution after 10 min ultrasonication; (3) the BNNT solution after 1 h ultrasonication. (c) Representative HRTEM images of double-walled (DW), triple-walled (TW), and quadruple-walled (QW) BNNTs. (d) The respective outer diameter ranges for BNNTs of one to four walls captured by HRTEM. (e) (Top) Tapping-mode AFM image of one dispersed BNNT on a silicon substrate with a height of 2.9 nm. (Bottom) Schematic of the cross-section of one DW-BNNT on a flat substrate. (f) (Top) HRTEM image of one DW-BNNT with significant radial contraction deformation. (Bottom) The digitized conformation of this tube showing the wall deformation.

diameter region(s). The upper image in figure 1(e) shows a representative tapping-mode AFM image of one dispersed BNNT deposited on a clean Si substrate with an original tube cross-section height (h_0) of 2.9 nm. The outer diameter of this tube ($D_{\rm nt}^{\rm out}$) is estimated to be about 2.56 nm by considering $D_{\rm nt}^{\rm out} = h_0 - t$ [45], in which $t = 0.34$ nm is the inter-layer distance of the B–N sheet [23]. Therefore, the tube shown in the AFM image is most probably a DW-BNNT.

Occasionally, the microscopic structures of BNNTs with significant radial deformations were captured by HRTEM. The top image in figure 1(f) shows the structure of one DW-BNNT ($D_{nt}^{out} = 2.8$ nm) under bending deformation with a bending angle of 34°, which probably came into being during the nanotube post-processing processes. It can be seen that significant tube radial contraction deformation occurs along its transverse direction as a result of the bending of the tube, which can be ascribed to the bending-induced contraction and stretching of B–N bonds in the tube layers. There is no discernable evidence of the broken or fractured B–N layer around the tube radial contraction site, indicating that there is no breaking of B–N bonds or re-arrangement of boron and nitrogen atoms during the radial deformation of the tube. The observed morphology of this deformed tube is consistent with the previously reported findings of bending deformations of SW-BNNTs using molecule dynamics (MD) simulations [27]. The bottom plot in figure 1(f) shows the digitized tube conformation based on the recorded HRTEM image. The inner diameter of the tube at the undeformed positions is measured to be about 2.1 nm, while the closest distance between the inner walls at the radial contraction site is measured to be about 0.4 nm, which is very close to the inter-layer distance of the B–N sheet, 0.34 nm [23]. It is noted that the inter-layer distance at the contraction site is noticeably smaller, although very difficult to quantify, compared to those at the undeformed positions, indicating that the inter-layer interaction is also squeezed when the tube is deformed along its transverse direction. It has been reported recently that rippling was observed on the tube layers of buckled MW-BNNTs in bending experiments. However, no ripple is observed on both the inner and outer tube layers for the DW-BNNT shown in figure 1(f), which can be ascribed to the fact that the diameter of this tube is small enough such that the contraction and stretching of B–N bonds are able to accommodate the bending-induced morphology change. The observed significant radial contraction deformation when the tube is under modest bending suggests that BNNTs are of high flexibility in its transverse direction, which is consistent with several recently reported experimental observations [9, 17, 46].

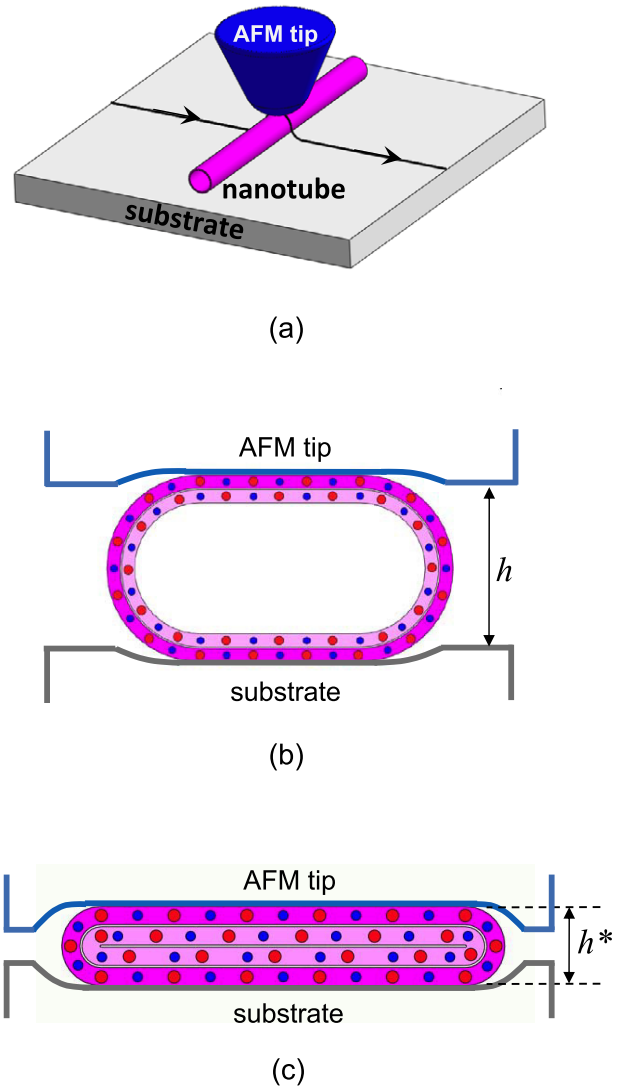

Figure 2. (a) Schematic of the AFM-based compression testing scheme on the radial deformation of an individual BNNT on a flat substrate. (b) Schematic of the deformations of a double-walled nanotube, an AFM tip and a substrate along the nanotube's transverse direction under relatively small compressive loads. (c) Schematic of the nanotube cross-section conformation under large compressive loads where the two opposing nanotube faces are in close proximity. Red and blue dots represent nitrogen and boron atoms in the nanotube, respectively. All drawings are not to scale.

2.2. AFM-based BNNT radial elasticity measurements

Radial mechanical deformations of individual MW-BNNTs were characterized using AFM-based compression testing techniques as illustrated by figure 2(a) (see section 4 for details). This nanomechanical testing technique was previously employed in studying the radial elasticity of SW-BNNTs [17] as well as single-walled and multi-walled CNTs [47–50]. Figures 2(b) and (c) illustrate the cross-section deformation of the nanotube, the AFM tip and the substrate under relatively small and large compressive loads, respectively.

Figure 3(a) shows three selected AFM line-scanning profiles measured on one BNNT, as shown in the inset AFM image, recorded in contact mode at compressive loads of 0.05, 3 and 5 nN, respectively. Prominent nanotube cross-section height reduction, which increases with the compressive load, is observed. The well-overlapping of the nanotube position in all three profiles indicates that the nanotube remained at a standstill on the substrate during the compressive test for the given load range. Figure 3(b) shows the measured nanotube height (h) and the corresponding measurement error as a function of the compressive load (P) for the tube shown in figure 3(a).

Figure 4(a) shows the repeated loading and unloading profiles of one BNNT with an original tube cross-section height of about 4.5 nm. The measurements on the BNNT height as a function of the compressive load are based on four compression and three decompression tests that were executed alternately and consecutively. The overlapping of

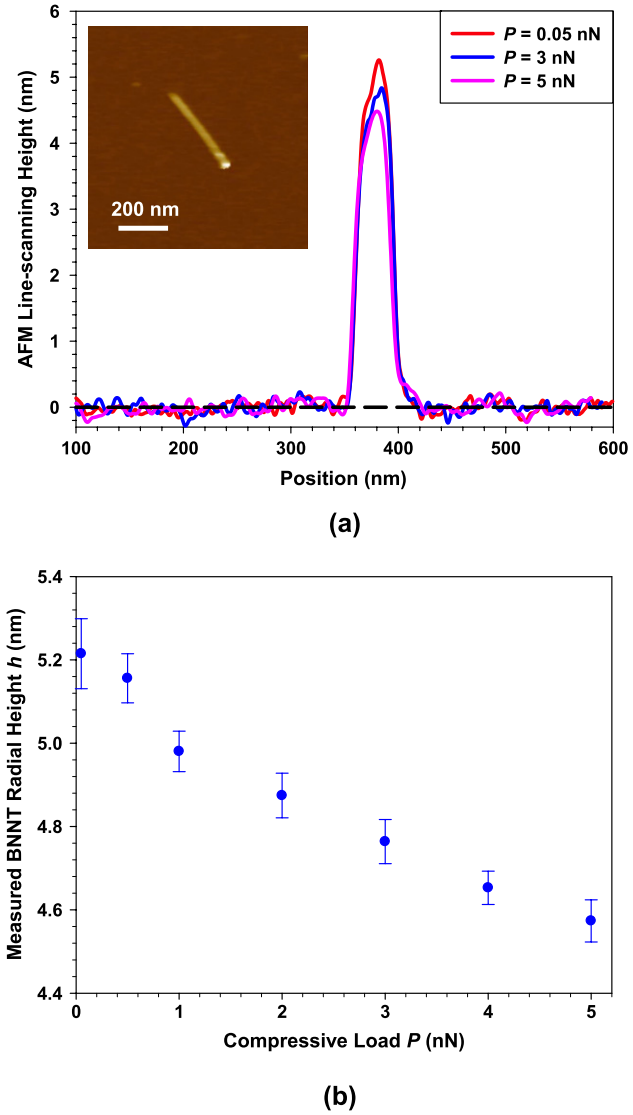

Figure 3. (a) Selected contact-mode AFM line-scanning profiles measured on a BNNT with an original tube cross-section height on the substrate of about 5.22 nm. The inset shows a contact-mode AFM image (the set-point is 0.05 nN) of this measured tube. (b) The measured height–load profile for the tube shown in (a). The error bars for the nanotube height are measured based on the portions of the scanning profiles in the vicinity of the nanotube.

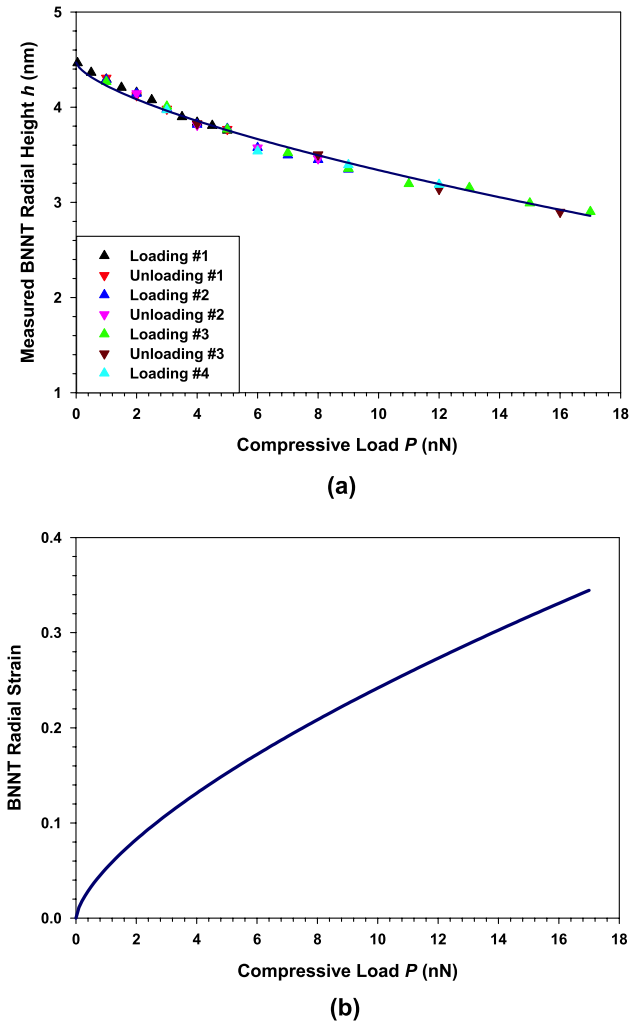

Figure 4. (a) Repeated loading (triangle-up points) and unloading (triangle-down points) curves recorded on one BNNT with $h_0 = 4.5$ nm. The solid line represents the fitting curve to the experimental data based on the Hertzian model. (b) Theoretical prediction of the corresponding radial strain versus the compressive load for the BNNTs shown in (a).

the loading and unloading curves indicates a purely elastic deformation in the tube transverse direction within the applied load range (up to 17 nN). The measured cross-section height of this tube at $P = 17$ nN is 2.9 nm, representing a height reduction of 35.6%. We want to emphasize here that the measured tube cross-section height reduction is ascribed not only to the radial deformation of the BNNT, but also to the deformations of the AFM tip and the substrate, as illustrated in figure 2(b). The net BNNT radial deformation is actually smaller than the measured tube height reduction. Neglecting the deformations of the AFM tip and the substrate effectively results in over-estimation of the BNNT radial deformation. It is noted that the presented radial deformation profiles were acquired with the tested BNNTs remaining at a standstill on the substrate during the whole testing process, which can be discerned from their consecutively recorded AFM scanning topography profiles as shown in figure 3(a). Our measurements were terminated when the tested BNNTs were found to be moved by the AFM tip on the substrate, which is most likely due to the fact that the adhesion between the nanotube and the substrate could not balance the lateral force exerted on the nanotube by the AFM probe.

To better understand the radial elasticity of the tested BNNTs, we interpret our nanomechanical measurement using Hertzian contact mechanics models (see section 4 for details). The contacts between the AFM tip, the BNNT, and the substrate are simplified as an elastic and friction-free nanoindentation system consisting of a spherical tip, a cylindrical tube, and a flat substrate. In this model, we consider cylindrical hollow BNNTs as elastic bodies, and their effective radial elastic moduli ($E_{\mathrm{nt}}^{\mathrm{rad}}$) are expected to be positively correlated to the rigidity of the tube cross-section and are determined by both the tube outer diameter and the number of tube layers. Since the strain energy in a

Table 1. Summarized measurements and calculations on six different BNNTs that were tested by first applying compressive loads of 0.05–5 nN, and then compressive loads of 50 nN. The actual tube height under compressive loads of 50 nN is calculated as the measured height plus the combined deformation of the AFM tip and the substrate.

Sample #	Original tube cross-section height (nm)	Measured tube height at $P = 50$ nN (nm)	Effective radial elastic modulus (GPa)	Combined AFM tip and substrate deformation at $P = 50$ nN (nm)	Actual tube height at $P = 50$ nN (nm)	Assigned number of tube layers
1	2.48	0.95	14.69	0.60	1.55	2
2	3.56	0.91	5.38	0.50	1.41	2
3	3.64	1.01	2.85	0.49	1.50	2
4	3.96	1.48	10.42	0.47	1.95	3
5	4.00	1.54	10.16	0.47	2.01	3
6	5.70	2.32	7.85	0.39	2.71	4

single-walled tube is inversely proportional to its diameter square, E_{nt}^{rad} of a MW-BNNT is expected to decrease with the increase of its outer diameter while increasing with its number of tube layers.

The solid line in figure 4(a) represents the fitting curve based on the Hertzian model for the experimental measurements, which displays very good agreement. Based on the curve fitting, the effective radial elastic moduli of the tested BNNTs are calculated to be 3.2 GPa. The diametrical deformation of the tube along the load direction (δd) can be calculated based on the Hertzian model by assuming that both the AFM tip and the substrate are rigid. Figure 4(b) shows the dependences of the radial strain ε_{nt}^{rad}, defined as $\varepsilon_{nt}^{rad} = \delta d/h_0$, on the applied load for the BNNT shown in figure 4(a). Our results show that the net radial strain for the BNNT reaches 34.5% at $P = 17$ nN, indicating that the combined deformation of the AFM tip and the substrate is merely 3.2% of the net tube radial deformation. The tube deformation dominates in all the deformational components in the measured tube height h because its effective radial elastic modulus is significantly lower compared with the elastic moduli of the AFM tip and the substrate. On the other hand, the deformations of the AFM tip and the substrate may be substantial if the tube's effective radial elastic modulus is comparable to their elastic moduli. In such cases, neglecting the deformation of the AFM tip and/or the substrate in the Hertzian model may results in significant under-estimation of the effective radial elastic moduli of the tested BNNTs.

As mentioned previously, the radial rigidity of MW-BNNTs depends on both the tube outer diameter and the number of tube walls. While the tube outer diameter can be readily quantified by AFM, the quantification of the tube wall number using AFM is not a straightforward task. It is known that the tube cross-section gets flattened (see figure 2(c)) when it is subjected to large compressive loads (e.g. 50 nN) and the cross-section height of a completely flattened tube (h^* in figure 2(c)) is nearly proportional to its number of tube layers [45, 51]. According to our experimental observation shown in figure 1(f), the inter-layer distance of a radially compressed BNNT is considered to be largely unchanged with a value of about 0.34 nm. Therefore, the cross-section heights of completely flattened single- to quadruple-walled BNNTs are expected to be about 0.68, 1.36, 2.04, and 2.72 nm, respectively. We performed the nanotube flattening experiments on six different BNNTs with

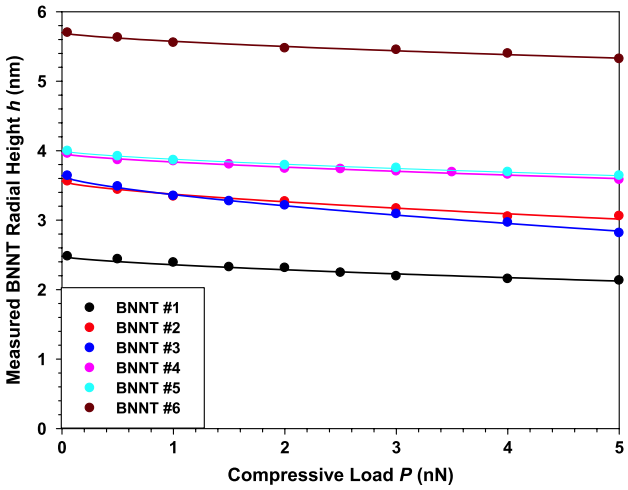

Figure 5. The respective radial deformation profiles of six different BNNTs. The solid lines are the respective fitting curves of the experimental data based on the Hertzian model. The effective radial moduli of these tested tubes are listed in table 1.

original tube heights (h_0) from 2.48 to 5.70 nm. The radial deformation of these BNNTs was first measured individually under compressive loads of up to 5 nN, from which their respective effective radial moduli were calculated. The radial deformation measurements and the respective fitting curves based on the Hertzian model are presented in figure 5. Then their respective heights on the substrate under compressive loads of 50 nN were measured. As discussed previously, the measured tube height (h) is smaller than the actual tube height due to the deformation of the AFM tip and the substrate. The combined deformation of the AFM tip and the substrate at $P = 50$ nN for each tube measurement is estimated using the Hertzian contact mechanics model by assuming that the BNNT is a rigid body. The actual flattened tube height at $P = 50$ nN is calculated as the measured tube height plus the combined deformation of the AFM tip and the substrate. All the measured and calculated values on these six BNNTs are summarized in table 1. Among the six tested BNNTs, tubes #1–#3 are assigned to be DW-BNNTs, while tubes #4–#5 are TW-BNNTs and tube #6 is a QW-BNNT. We also want to highlight that the consistent results obtained on tubes #4 and #5 listed in table 1, which have almost identical

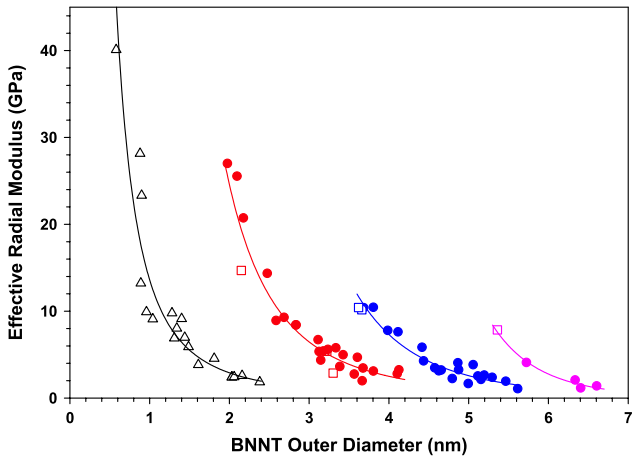

Figure 6. The dependence of the measured effective radial modulus of SW- and MW-BNNTs on the tube outer diameter. The triangular points represent experimental data for SW-BNNTs, which are reproduced from [17]. The square points represent the data measured on those tubes listed in table 1. The solid lines are power-function fitting curves of the respective experimental data sets.

outer diameters, demonstrate the good reproducibility of our AFM-based nanomechanical measurements.

Figure 6 shows the BNNT effective radial modulus as a function of the tube outer diameter based on measurements of 53 different BNNTs with outer diameters ranging from 2.0 to 6.6 nm, which are shown in red, blue, and pink points. It can be clearly seen from figure 6 that these measured data points form three distinct groups of data sets, each of which shows a decreasing trend with the increase of outer tube diameter and can be reasonably well fitted by power functions (solid curves). For the purpose of comparison, figure 6 also includes the recently reported experimental data on SW-BNNTs [17] (black triangular points), which were obtained using the same experimental and theoretical protocols and approaches as the present work. From the data values and their trends shown in figure 6, we reasonably believe that the red points correspond to DW-BNNTs, while the blue and the pink points correspond to TW-BNNTs and QW-BNNTs, respectively. The outer diameters of the measured tubes corresponding to each number of tube walls are consistent with our HRTEM measurements as shown in figure 1(d). It is noted that the measured data for tubes with known tube wall numbers, which are listed in table 1 and shown in figure 6 as square points, follow their respective trends very well, supporting our classification of the tested BNNTs by their tube wall numbers.

It is noticed from the red data set that the effective radial moduli of DW-BNNTs with outer diameters from 2.0 to 2.5 nm are found to decrease from 27 to 14.3 GPa, which are several-fold higher than those of SW-BNNTs within the same diameter range (i.e. 2.4–1.9 GPa for diameters from 2.0 to 2.4 nm), implying that DW-BNNTs of higher radial rigidity more readily undertake a circular cross-section in bundle and yarn structures or when they are in contact with other materials surfaces compared with SW-BNNT of lower radial rigidity. Similar differences are also observed in the comparison of the effective radial moduli among DW, TW, and QW-BNNTs. It is also noticed from figure 6 that the distances between the two neighboring fitting curves at given elastic moduli are consistently larger than 0.68 nm, the increase of the tube outer diameter with the increase of one tube layer. Our results unambiguously demonstrate that the BNNT radial rigidity increases with the number of tube walls, while decreasing with the tube outer diameter.

It is desirable to compare the radial elastic moduli of MW-BNNTs with those of MW-CNTs in the same diameter and number of tube walls range. However, systematic measurements on the radial elasticity of small diameter MW-CNTs are still not available even though some values were reported in the literature that are mostly for large-diameter tubes and, in most cases, without the exact known numbers of tube layers or interpreted using different contact mechanics models [48, 50–52]. Therefore, a meaningful comparison of the radial elasticity of these two types of similar nanostructures is still not available. We want to mention that a systematic and quantitative study on the radial elasticity of double- and triple-walled CNTs by employing the same experimental and theoretical approaches presented in this paper is currently being conducted by our group and will be reported in future publications.

2.3. Future model improvements

We want to point out that the BNNTs undergo complex deformation processes during our AFM-based compression tests, which involve bending, stretching, and rotation of the B–N bonds in the nanotube. The employed contact mechanics model is a simplified continuum model that takes into account the deformations of all the contacting elements in our testing system (i.e. the AFM tip, the nanotube, and the substrate) based on their simplified geometries and contacting interfaces. While this simplified model helps to facilitate the interpretation of our experimental measurements, it may also result in deviations, or even substantial inaccuracy, in the quantification of the radial deformability of the nanotubes. Below we briefly summarize the key simplifications and assumptions on which the present contact mechanics model is based, and provide some guidelines about how to improve the current model for future work. First, the cross-section of the nanotube on the flat substrate is assumed to be perfectly circular, thus neglecting the cross-section flattening effect due to its van der Waals interaction with the substrate. This cross-section flattening effect becomes particularly severe for large-diameter nanotubes [24]. Second, only the native oxide layer of the Si substrate is considered in the present model, while the deformation of the bulk Si underneath the oxide layer is neglected. Third, the present model does not take into account the effect of the friction force between the AFM tip and the nanotube in modeling the deformations of both the AFM tip and the nanotube. Fourth, the deformed shapes of the AFM tip and the nanotube, as illustrated in figure 2(b), likely deviate substantially from their assumed spherical and cylindrical shapes respectively. All these factors are essential for a more precise theoretical model that enables

the interpretation of our experimental measurements in a more realistic setting. It is noted that it would be an intractable, if not impossible, task to devise an analytical model to account for all the above-mentioned geometric corrections and the friction force component in the analysis of the radial deformation of the nanotube. Therefore, new theoretical models based on advanced computational approaches, such as finite element methods (FEM) and molecular dynamics (MD), are warranted to further investigate the radial deformation of BNNTs compressed by AFM probes and provide a more precise quantification of their radial deformability.

3. Concluding remarks

In this paper, we present a nanoscale experimental study of the radial mechanical properties of MW-BNNTs synthesized by PVC methods. The effectiveness of ionic surfactant NaDDBS in dispersing PVC-synthesized BNNTs was demonstrated. Our AFM-based nanomechanical measurements reveal the radial elasticity of MW-BNNTs, including their effective radial elastic moduli. Our results clearly show that DW-BNNTs have much higher effective radial moduli than SW-BNNT within the same diameter range. Particularly, our measurements directly identify the correlation between the measured effective radial moduli of BNNTs with both their outer diameters and their numbers of tube layers. Our results reported in this paper help us to understand the resisting capacity of BNNTs to transverse loads and their cross-section configurations in bundle and yarn structures, or when they are in contact with other materials surfaces, and thus contribute directly to a complete understanding of their fundamental structural and material properties and the pursuit of their novel structural and electronics applications.

4. Experiments and methods

4.1. BNNT sample preparation

The employed BNNTs were synthesized using a pressurized vapor/condenser (PVC) method and were confirmed to possess highly crystalline, very thin and long structures [23]. As-synthesized BNNTs were separated in deionized (DI) water by ultrasonication for 1–2.5 h with the aid of sodium dodecylbenzenesulfonate (NaDDBS) purchased from Sigma-Aldrich, Co. After centrifugation at 2000 rpm, small drops from the top portion of the BNNT solution were deposited on clean Si wafers or copper grids with lacey support films (Ted Pella, Inc.) and then repeatedly washed using DI water to remove residue surfactants. BNNT samples were then air-dried for TEM and AFM measurements.

4.2. TEM characterization

The high resolution transmission electron microscopy (HRTEM) characterization of BNNTs was performed using a JEM 2100F TEM (JEOL Ltd) operated at accelerating voltages of 120–200 kV.

4.3. AFM characterization

All AFM imaging and nanomechanical measurements were performed using a Park Systems XE-70 AFM at room temperature in ambient environment. The employed AFM is incorporated with a closed-loop feedback control feature in *XYZ* axes. Tapping-mode AFM was performed using silicon AFM probes (model T-190, VistaProbe) with a nominal spring constant of 48 N m^{-1}. Contact-mode AFM measurements were performed using silicon AFM cantilevers (model CSG 11, NT-MDT) with nominal spring constants of 0.01–0.08 N m^{-1}. The actual spring constant of each employed CSG 11 AFM cantilever was calibrated using the thermal tuning method based on equipartition theory [53, 54] and was found to be in the range of 0.04–0.09 N m^{-1}. The thermal-induced rms deflection noise of the employed AFM probes at the tip position in the 1–500 Hz bandwidth was measured to be 0.71 Å, and the corresponding rms force noise is calculated to be about 3–7 pN. For the BNNT radial elasticity measurements, as illustrated by figure 2(a), the silicon AFM tip is controlled to scan an individual BNNT on the substrate in contact mode at a specified compressive load with the scanning direction perpendicular to the tube axis. The employed AFM scanning rate and scanning length were 50 nm s^{-1} and 400–800 nm, respectively. The applied compressive load is calculated as the product of the spring constant of the AFM probe and its vertical deflection that was measured with sub-angstrom resolutions using laser-reflection schemes. The closed-loop feedback control feature of the employed AFM enables angstrom-level positioning resolutions and allows repeated contact-mode scanning of the same position on one BNNT at a variety of compressive loads.

4.4. Hertzian contact mechanics modeling

In our measurement, the BNNT's radial deformation under a compressive load is considered to be a quasi-static process. The measured cross-section height (h, see figure 2(b)) of a BNNT on a flat Si substrate under a compressive load P is given by [17, 47]

$$\begin{aligned} h &= 2h_0 - \left(\frac{P}{k_1\sqrt{h_0}}\right)^{2/3} - \left(\frac{P}{k_2\sqrt{[1/h_0 + 1/R_{\text{tip}}]^{-1}}}\right)^{2/3} \\ &\quad + \left(\frac{P}{k_3\sqrt{R_{\text{tip}}}}\right)^{2/3}, \\ k_1 &= \frac{4}{3}\left(\frac{1-\nu_{\text{nt}}^2}{E_{\text{nt}}^{\text{rad}}} + \frac{1-\nu_{\text{sub}}^2}{E_{\text{sub}}}\right)^{-1}, \\ k_2 &= \frac{4}{3}\left(\frac{1-\nu_{\text{tip}}^2}{E_{\text{tip}}}\right)^{-1}, \\ k_3 &= \frac{4}{3}\left(\frac{1-\nu_{\text{tip}}^2}{E_{\text{tip}}} + \frac{1-\nu_{\text{sub}}^2}{E_{\text{sub}}}\right)^{-1}, \end{aligned} \tag{1}$$

where E and ν represent the elastic modulus (effective radial elastic modulus for BNNTs) and the Poisson's ratio,

respectively, for materials of BNNTs (subscript-nt), AFM tips (tip), and substrates (sub). On the right side of equation (1), the second term represents the deformations of both the nanotube and the substrate due to the nanoindentation of the nanotube–substrate system. The third term represents the deformation of the AFM tip due to its contact with the nanotube, in which the nanotube is considered as a rigid body to avoid double-counting its deformation. The last term represents the deformation of the Si substrate due to the nanoindentation of the AFM tip. A native oxide layer of ∼2 nm in thickness was measured on the surface of the Si substrates using ellipsometry (Model Uvisel, Horiba, Ltd). We reasonably assume similar oxide layers on the surface of the employed silicon AFM tips [55]. The materials for both the AFM tip and the substrate are considered to be native silicon oxide with an elastic modulus of 74 GPa and a Poisson's ratio of 0.16, while a Poisson's ratio $\nu_{nt} = 0.2$ is considered for BNNTs in the present Hertzian model [17]. h_0 represents the original cross-section height of the nanotube on the substrate and is estimated through fitting and interpolation of the measured height h versus the applied load P curve to zero load using power functions. The radius of curvature of the employed AFM tips, R_{tip}, is estimated to be about 25 nm based on the geometrical deconvolution relationship $R_{tip} = \omega^2/8\Delta$, in which Δ and ω are the measured height and the apparent width of a nanotube in the AFM scanning image [56]. In our data analysis, we assume that the tested BNNTs undertake circular cross-sections on the substrate, and neglect the effect of van der Waals interactions between the nanotube and the substrate on the flattening of the nanotube cross-section [24]. It is noted that the Hertzian model does not take into account the nanotube deformations caused by the friction forces among all the elastic components, which are assumed to be much smaller compared with the deformations caused by the compressive load.

Acknowledgments

This work was funded by US Air Force Office of Scientific Research—low density materials program under Grant Nos FA9550-11-1-0042 and FA9550-10-1-0451, and was also partially supported by American Chemistry Society-Petroleum Research Fund. The SEM and HRTEM characterizations were performed using the facilities in the Analytical and Diagnostics Laboratory at Binghamton University's Small Scale Systems Integration and Packaging Center (S^3IP).

References

[1] Rubio A, Corkill J L and Cohen M L 1994 Theory of graphitic boron-nitride nanotubes *Phys. Rev.* B **49** 5081–4
[2] Chopra N G, Luyken R J, Cherrey K, Crespi V H, Cohen M L, Louie S G and Zettl A 1995 Boron-nitride nanotubes *Science* **269** 966–7
[3] Wei X L, Wang M S, Bando Y and Golberg D 2010 Tensile tests on individual multi-walled boron nitride nanotubes *Adv. Mater.* **22** 4895–9
[4] Chopra N G and Zettl A 1998 Measurement of the elastic modulus of a multi-wall boron nitride nanotube *Solid State Commun.* **105** 297–300
[5] Arenal R, Wang M S, Xu Z, Loiseau A and Golberg D 2011 Young modulus, mechanical and electrical properties of isolated individual and bundled single-walled boron nitride nanotubes *Nanotechnology* **22** 265704
[6] Hernandez E, Goze C, Bernier P and Rubio A 1998 Elastic properties of C and $B_xC_yN_z$ composite nanotubes *Phys. Rev. Lett.* **80** 4502–5
[7] Suryavanshi A P, Yu M F, Wen J G, Tang C C and Bando Y 2004 Elastic modulus and resonance behavior of boron nitride nanotubes *Appl. Phys. Lett.* **84** 2527–9
[8] Golberg D, Costa P M F J, Lourie O, Mitome M, Bai X D, Kurashima K, Zhi C Y, Tang C C and Bando Y 2007 Direct force measurements and kinking under elastic deformation of individual multiwalled boron nitride nanotubes *Nano Lett.* **7** 2146–51
[9] Ghassemi H M, Lee C H, Yap Y K and Yassar R S 2010 Real-time fracture detection of individual boron nitride nanotubes in severe cyclic deformation processes *J. Appl. Phys.* **108** 024314
[10] Xiao Y, Yan X H, Cao J X, Ding J W, Mao Y L and Xiang J 2004 Specific heat and quantized thermal conductance of single-walled boron nitride nanotubes *Phys. Rev.* B **69** 205415
[11] Chang C W, Fennimore A M, Afanasiev A, Okawa D, Ikuno T, Garcia H, Li D Y, Majumdar A and Zettl A 2006 Isotope effect on the thermal conductivity of boron nitride nanotubes *Phys. Rev. Lett.* **97** 085901
[12] Chen Y, Zou J, Campbell S J and Le Caer G 2004 Boron nitride nanotubes: pronounced resistance to oxidation *Appl. Phys. Lett.* **84** 2430–2
[13] Golberg D, Bando Y, Kurashima K and Sato T 2001 Synthesis and characterization of ropes made of BN multiwalled nanotubes *Scr. Mater.* **44** 1561–5
[14] Blase X, Rubio A, Louie S G and Cohen M L 1994 Stability and band-gap constancy of boron-nitride nanotubes *Europhys. Lett.* **28** 335–40
[15] Lee C H, Xie M, Kayastha V, Wang J S and Yap Y K 2010 Patterned growth of boron nitride nanotubes by catalytic chemical vapor deposition *Chem. Mater.* **22** 1782–7
[16] Golberg D, Bando Y, Huang Y, Terao T, Mitome M, Tang C C and Zhi C Y 2010 Boron nitride nanotubes and nanosheets *ACS Nano* **4** 2979–93
[17] Zheng M, Chen X, Bae I-T, Ke C, Park C, Smith M W and Jordan K 2012 Radial mechanical properties of single-walled boron nitride nanotubes *Small* **8** 116–22
[18] An L N *et al* 2004 Carbon-nanotube-reinforeed polymer-derived ceramic composites *Adv. Mater.* **16** 2036–40
[19] Golberg D, Bando Y, Dorozhkin P and Dong Z C 2004 Synthesis, analysis, and electrical property measurements of compound nantubes in the B–C–N ceramic system *MRS Bull.* **29** 38–42
[20] Bansal N P, Hurst J B and Choi S R 2006 Boron nitride nanotubes-reinforced glass composites *J. Am. Ceram. Soc.* **89** 388–90
[21] Huang Q, Bando Y S, Xu X, Nishimura T, Zhi C Y, Tang C C, Xu F F, Gao L and Golberg D 2007 Enhancing superplasticity of engineering ceramics by introducing BN nanotubes *Nanotechnology* **18** 485706
[22] Lopez M J, Rubio A, Alonso J A, Qin L C and Iijima S 2001 Novel polygonized single-wall carbon nanotube bundles *Phys. Rev. Lett.* **86** 3056–9
[23] Smith M W, Jordan K C, Park C, Kim J W, Lillehei P T, Crooks R and Harrison J S 2009 Very long single- and few-walled boron nitride nanotubes via the pressurized vapor/condenser method *Nanotechnology* **20** 505604

[24] Hertel T, Walkup R E and Avouris P 1998 Deformation of carbon nanotubes by surface van der Waals forces *Phys. Rev.* B **58** 13870–3
[25] Song J, Huang Y, Jiang H, Hwang K C and Yu M F 2006 Deformation and bifurcation analysis of boron-nitride nanotubes *Int. J. Mech. Sci.* **48** 1197–207
[26] Song J, Wu J, Huang Y and Hwang K C 2008 Continuum modeling of boron nitride nanotubes *Nanotechnology* **19** 445705
[27] Enyashin A N and Ivanovskii A L 2006 Deformation mechanisms for carbon and boron nitride nanotubes *Inorg. Mater.* **42** 1336–41
[28] Bai X D, Golberg D, Bando Y, Zhi C Y, Tang C C, Mitome M and Kurashima K 2007 Deformation-driven electrical transport of individual boron nitride nanotubes *Nano Lett.* **7** 632–7
[29] Kinoshita Y and Ohno N 2010 Electronic structures of boron nitride nanotubes subjected to tension, torsion, and flattening: a first-principles DFT study *Phys. Rev.* B **82** 085433
[30] Zhi C Y, Bando Y, Tang C C and Golberg D 2010 Boron nitride nanotubes *Mater. Sci. Eng.* R **70** 92–111
[31] Su C Y, Juang Z Y, Chen K F, Cheng B M, Chen F R, Leou K C and Tsai C H 2009 Selective growth of boron nitride nanotubes by the plasma-assisted and iron-catalytic CVD methods *J. Phys. Chem.* C **113** 14681–8
[32] Lourie O R, Jones C R, Bartlett B M, Gibbons P C, Ruoff R S and Buhro W E 2000 CVD growth of boron nitride nanotubes *Chem. Mater.* **12** 1808–10
[33] Chen Y, Chadderton L T, FitzGerald J and Williams J S 1999 A solid-state process for formation of boron nitride nanotubes *Appl. Phys. Lett.* **74** 2960–2
[34] Golberg D, Bando Y, Eremets M, Takemura K, Kurashima K and Yusa H 1996 Nanotubes in boron nitride laser heated at high pressure *Appl. Phys. Lett.* **69** 2045–7
[35] Yu D P, Lee C S, Bello I, Sun X S, Tang Y H, Zhou G W, Bai Z G, Zhang Z and Feng S Q 1998 Synthesis of nano-scale silicon wires by excimer laser ablation at high temperature *Solid State Commun.* **105** 403–7
[36] Laude T, Matsui Y, Marraud A and Jouffrey B 2000 Long ropes of boron nitride nanotubes grown by a continuous laser heating *Appl. Phys. Lett.* **76** 3239–41
[37] Arenal R, Stephan O, Cochon J L and Loiseau A 2007 Root-growth mechanism for single-walled boron nitride nanotubes in laser vaporization technique *J. Am. Chem. Soc.* **129** 16183–9
[38] Zhi C Y, Bando Y, Terao T, Tang C C, Kuwahara H and Golberg D 2009 Towards thermoconductive, electrically insulating polymeric composites with boron nitride nanotubes as fillers *Adv. Funct. Mater.* **19** 1857–62
[39] Li Y B, Dorozhkin P S, Bando Y and Golberg D 2005 Controllable modification of SiC nanowires encapsulated in BN nanotubes *Adv. Mater.* **17** 545–9
[40] Chen Z G, Zou J, Liu G, Li F, Cheng H M, Sekiguchi T, Gu M, Yao X D, Wang L Z and Lu G Q 2009 Long wavelength emissions of periodic yard-glass shaped boron nitride nanotubes *Appl. Phys. Lett.* **94** 023105
[41] Matarredona O, Rhoads H, Li Z R, Harwell J H, Balzano L and Resasco D E 2003 Dispersion of single-walled carbon nanotubes in aqueous solutions of the anionic surfactant NaDDBS *J. Phys. Chem.* B **107** 13357–67
[42] Clark M D, Subramanian S and Krishnamoorti R 2011 Understanding surfactant aided aqueous dispersion of multi-walled carbon nanotubes *J. Colloid Interface Sci.* **354** 144–51
[43] Islam M F, Rojas E, Bergey D M, Johnson A T and Yodh A G 2003 High weight fraction surfactant solubilization of single-wall carbon nanotubes in water *Nano Lett.* **3** 269–73
[44] Yu J, Chen Y and Cheng B M 2009 Dispersion of boron nitride nanotubes in aqueous solution with the help of ionic surfactants *Solid State Commun.* **149** 763–6
[45] DeBorde T, Joiner J C, Leyden M R and Minot E D 2008 Identifying individual single-walled and double-walled carbon nanotubes by atomic force microscopy *Nano Lett.* **8** 3568–71
[46] Ghassemi H M, Lee C H, Yap Y K and Yassar R S 2011 *In situ* observation of reversible rippling in multi-walled boron nitride nanotubes *Nanotechnology* **22** 115702
[47] Yang Y H and Li W Z 2011 Radial elasticity of single-walled carbon nanotube measured by atomic force microscopy *Appl. Phys. Lett.* **98** 041901
[48] Palaci I, Fedrigo S, Brune H, Klinke C, Chen M and Riedo E 2005 Radial elasticity of multiwalled carbon nanotubes *Phys. Rev. Lett.* **94** 175502
[49] Barboza A P M, Chacham H and Neves B R A 2009 Universal response of single-wall carbon nanotubes to radial compression *Phys. Rev. Lett.* **102** 025501
[50] Yu M F, Kowalewski T and Ruoff R S 2000 Investigation of the radial deformability of individual carbon nanotubes under controlled indentation force *Phys. Rev. Lett.* **85** 1456–9
[51] Minary-Jolandan M and Yu M F 2008 Reversible radial deformation up to the complete flattening of carbon nanotubes in nanoindentation *J. Appl. Phys.* **103** 073516
[52] Muthaswami L, Zheng Y, Vajtai R, Shehkawat G, Ajayan P and Geer R E 2007 Variation of radial elasticity in multiwalled carbon nanotubes *Nano Lett.* **7** 3891–4
[53] Florin E L, Rief M, Lehmann H, Ludwig M, Dornmair C, Moy V T and Gaub H E 1995 Sensing specific molecular-interactions with the atomic-force microscope *Biosens. Bioelectron.* **10** 895–901
[54] Ke C, Humeniuk M, S-Gracz H and Marszalek P E 2007 Direct measurements of base stacking interactions in DNA by single-molecule atomic-force spectroscopy *Phys. Rev. Lett.* **99** 018302
[55] Souha H, Viale D, Weber G and Gillot B 1989 Effects of a silicon-oxide layer on reactivity of silicon with copper(I) chloride *J. Mater. Sci.* **24** 1767–71
[56] Gibson C T, Watson G S and Myhra S 1997 Scanning force microscopy—calibrative procedures for 'best practice' *Scanning* **19** 564–81